Available online at www.sciencedirect.com
ScienceDirect
Trans. Nonferrous Met. Soc. China 31(2021) 1031−1048
Transactions of Nonferrous Metals Society of China
www.tnmsc.cn

Tailoring microstructure and microhardness of Zn−1wt.%Mg−(0.5wt.%Mn, 0.5wt.%Ca) alloys by solidification cooling rate

Talita A. VIDA[1], Cássio A. P. SILVA[1], Thiago S. LIMA[1], Noé CHEUNG[1], Crystopher BRITO[2], Amauri GARCIA[1]

1. Department of Manufacturing and Materials Engineering, University of Campinas-UNICAMP, Campinas 13083-860, SP, Brazil;
2. Campus of São João da Boa Vista, São Paulo State University-UNESP, São João da Boa Vista 13876-750, SP, Brazil

Received 14 May 2020; accepted 30 November 2020

Abstract: Biodegradable Zn-based alloys, particularly Zn−Mg alloys with the addition of alloying elements, have been intensively investigated aiming to improve both mechanical properties and corrosion behavior. Since such properties are strongly dependent on the alloy microstructure, any evaluation should commence on understanding the conditions influencing its formation. In this study, the effect of the solidification cooling rate on the microstructural evolution of Zn−1wt.%Mg−(0.5wt.%Ca, 0.5wt.%Mn) alloys during transient solidification was investigated. The results show that the microstructures of both alloys have three phases in common: η-Zn dendritic matrix, intermetallic compounds (IMCs) $Zn_{11}Mg_2$, and Zn_2Mg in the eutectic mixture. $MnZn_9$ and two Ca-bearing phases ($CaZn_{11}$ and $CaZn_{13}$) are associated with Mn and Ca additions, respectively. These additions are shown to refine the dendritic matrix and the eutectic mixture as compared to the Zn−1wt.%Mg alloy. A correlation between cooling rate, dendritic or eutectic spacings was developed, thus permitting experimental growth laws to be proposed. Additionally, hardness tests were performed to evaluate the effects of additions of Ca and Mn. Experimental correlations between Vickers microhardness and secondary dendritic spacings were proposed, showing that the microstructural refinement and characteristic Ca and Mn based IMCs induce an increase in hardness as compared to the binary alloy.
Key words: Zn−Mg−(Ca, Mn) alloys; solidification; cooling rate; microstructure; microhardness

1 Introduction

Zn and Mg are considered prospective metals with a view to applications in biodegradable bone implants. Mg alloys are considered to have mechanical strength near that of bone but, in contrast, the corrosion behavior is related to high degradation rates. On the other hand, Zn has a much higher corrosion resistance in physiological solutions as contrasted to Mg. The combined mechanical and corrosion characteristics of Zn−Mg alloys associated with the fact that Zn is a biologically acceptable element even alloyed to Mg, render Zn−Mg alloys interesting options to the manufacture of bioabsorbable devices [1−3].

YAO et al [4] examined the effects of alloy solute content on microstructure, microhardness and corrosion properties of Zn−Mg alloys prepared by a melting/casting process in a range of Mg from 1 to 5 wt.%. They reported a microstructure formed mainly by Zn, and the intermetallic compounds Mg_2Zn_{11} and $MgZn_2$, with the increase in the eutectic fraction for alloys of higher Mg content. The addition of Mg to Zn was shown to give more positive corrosion properties as compared to those of pure Zn and the best corrosion properties were related to the Zn−3wt.%Mg alloy, which presented

Corresponding author: Crystopher BRITO; E-mail: crystopher.brito@unesp.br
DOI: 10.1016/S1003-6326(21)65559-0

a Vickers microhardness of about 165 HV as compared to 43.4 HV for Zn. VIDA et al [5] used a transient directional solidification technique to examine the effects of solidification thermal parameters on microstructural features and the length scale of the representative phases of the as-solidified microstructure of Zn−Mg alloys having 0.3−1.2 wt.% Mg. They reported microstructures composed of a Zn-rich matrix characterized by plate-like cells for high cooling rates and by a granular/dendritic transition with the decrease in the cooling rate for 0.3 and 0.5 wt.% Mg alloys. In contrast, the Zn−1.2wt.%Mg alloy presented a completely dendritic microstructure along a range of cooling rates from 2 to 20 K/s. The eutectic was formed by a competitive mixture of Zn−$Zn_{11}Mg_2$ and Zn−Zn_2Mg phases of lamellar morphology for any cooling rate and Zn−Mg alloy examined.

It is known that microstructural features of alloys in large measure determine the resulting mechanical strength and chemical properties. In terms of as-solidified microstructures many factors affecting the resulting properties are linked to alloy composition, local solidification thermal parameters such as the growth rate (V) and the cooling rate ($\dot{T}$), competition between equilibrium and non-equilibrium phases, and morphology and length scales of the representative phases. Techniques of controlled solidification have been shown to permit appropriate mechanical and corrosion properties to be achieved by an adequate design of microstructural patterns based on the control of V and $\dot{T}$. The vertical upward transient directional solidification technique, in devices using a water-cooled bottom mold, has been reported as a useful technique to encompass in just one as-cast sample, with a wide range of V and $\dot{T}$ from bottom to top of the directionally solidified casting [6,7]. A number of recent studies have reported correlations between parametric features of the as-solidified microstructure and the resulting hardness [8,9], tensile strength [10], machinability [11], wear resistance [12], electrical properties [9,13] and corrosion resistance [14].

Other elements can also be added to Zn−Mg alloys with a view to the improved mechanical strength and corrosion properties; however, when intended for biomedical applications care should be exercised with respect to their toxicity. According to HERNÁNDEZ-ESCOBAR et al [15] appropriate alloying elements include nutrient elements such as Ca and Sr and essential elements for physiological actions, for example Cu and Mn. Considering the existing literatures [1−4,15] with respect to Zn−Mg−(Ca, Mn) alloys, experimental studies focusing on the evolution of different phases forming these alloys microstructures with the solidification cooling rate remain scarce. The present study aims to provide an improved comprehension on the interrelation of growth characteristics, morphology and length scales of the phases forming the microstructure of Zn−1wt.%Mg−(0.5wt.%Ca, 0.5wt.%Mn) alloys with variable experimental $\dot{T}$ values. A transient directional solidification technique is used, which is able to provide a wide range of $\dot{T}$ along the length of the alloy casting in a single experiment. Moreover, with a view to examining the connection between microstructure and mechanical properties, the length scale of a representative phase of microstructures in these alloys was correlated to the microhardness along the length of the experimental castings.

2 Experimental

The Zn−1wt.%Mg−0.5wt.%Mn and Zn−1wt.%Mg−0.5wt.%Ca alloys were prepared using commercially pure metals. The metals used to prepare these alloys were supplied by TED Metals Industry Trade and Sigma–Aldrich, and their compositions are shown in Table 1. The metals were melted in a silicon refractory crucible (coated with an alumina layer to avoid contamination) using an electric resistance furnace. Firstly, Zn was melted at a temperature of 650 °C, after stoichiometric amounts of Mg and Mn or Ca were added to the molten Zn. Subsequently, the molten metal was stirred with a stainless steel bar, coated with refractory cement, and oxides were removed from the molten metal. The alloy was poured into the stainless steel mold positioned in the directional solidification apparatus, which was previously coated with alumina, and subjected to forced argon gas flow to avoid both oxidation and loss of metal.

The solidification experiments were carried out in a water-cooled apparatus, which was designed to promote directional solidification under transient heat flow conditions. The details of

Table 1 Chemical compositions of metals used to prepare alloys (wt.%)

Element	Zn	Mg	Mn	Ca	Cr	Fe	Al	Pb	Si	S	P	Others
Zn	Bal.	−	−	−	−	<0.1	−	<0.1	<0.01	−	−	<0.3
Mg	<0.1	Bal.	0.01	−	0.01	0.01	0.11	−	−	−	−	<0.3
Mn	−	−	Bal.	−	−	0.01	−	−	−	<0.1	<0.1	−
Ca*	−	−	−	Bal.	−	−	−	−	−	−	−	<1%

* Ca, 99%, Sigma−Aldrich

experimental casting apparatus, melting and solidification procedures were described in a previous study [5]. The alloys were remelted in situ and the lateral electric heaters, as shown in Fig. 1(a), had their power controlled in order to achieve a desired melt superheat prior to solidification. The temperatures during solidification were recorded using K-type thermocouples with stainless steel sheaths (1.6 mm in diameter), connected to a Lynx data logger system. When the melt temperature reached 12.5% above the alloy liquidus temperature, the external heaters were disconnected and the water flow at the bottom of the container started, thus permitting the onset of solidification (Fig. 1(a)). Although the thermal gradient ahead the dendrite's tip (G) and the growth rate (V) are sometimes analyzed independently mainly in steady-state solidification studies [16−18], the cooling rate ($\dot{T}$), given by $\dot{T}=GV$, has been preferably applied for microstructural growth correlations in unsteady-state solidification studies [5−8,10,11], since it synthetizes the effects of both thermal parameters. In this sense, the use of different melt superheats may shift the occurrence of determined cooling rate to another position in the casting, which is not relevant for the present work, since the goal is to correlate the length scale of a representative phase of the alloy microstructure to the cooling rate.

The macrostructures of the alloys' castings analysed in the present work are essentially formed by equiaxed grains along the length of the directionally solidified (DS) castings, similar to that of a previous study by some of the present authors concerning a Zn−1wt.%Mg alloy [5]. Therefore, either transverse or longitudinal (parallel to the growth direction) sections would permit the same visualization of the microstructural pattern. In this work, selected transverse (perpendicular to the growth direction) samples were extracted from the DS castings at different positions from the metal/mold interface (Figs. 1(b) and (c)), ground with SiC papers up to 1200 grit, polished with diamond paste (3 and 1 μm) and then finely etched with an acid solution (10% nital) for 7 s to reveal the microstructure. The microstructures were analyzed by optical microscopy, using an Olympus inverted metallurgical microscope (model 41GX). Additional microstructural characterization was carried out by scanning electron microscopy (SEM, ZEISS-EVO-MA15) equipped with an energy-dispersive X-ray spectrometer (EDS, OXFORD-X-MAX). The secondary dendrite arm and interlamellar spacings (λ_2 and λ_{eut}, respectively) were measured on transverse sections of the castings, with λ_{eut} measured from SEM images (Fig. 1(d)). The intercept method [19] was employed to measure both λ_2 and λ_{eut}, in which a straight line of length L was divided by a number (n) of secondary dendrite arms or eutectic fibers.

Three samples, covering the entire range of cooling rates of each alloy casting were selected and subjected to X-ray diffraction (XRD) analyses. XRD was used to determine all the phases presented in the microstructure, by comparing the XRD patterns with crystallographic data from the Inorganic Crystal Structure Database (ICSD) [20]. A Panalytical X′pert Pro MRD XL diffractometer with a 2θ range from 20° to 90°, and Cu K_α radiation with a wavelength of λ=0.15406 nm, was used to determine all the phases forming the microstructures. The samples used for segregation analyses were the same used for microstructure analyses. Such analyses were performed in a fluorescence spectrometer (XRF), model Rigaku RIX−3100 in order to estimate local average solute concentrations through an area of 100 mm^2 probe.

Vickers microhardness was tested according to the ASTM E92—16 standard [21], on the cross-sections of the samples using a load of 4.9 N and a dwell time of 15 s. The adopted hardness value of a representative position was the average of at least 20 measurements on each sample.

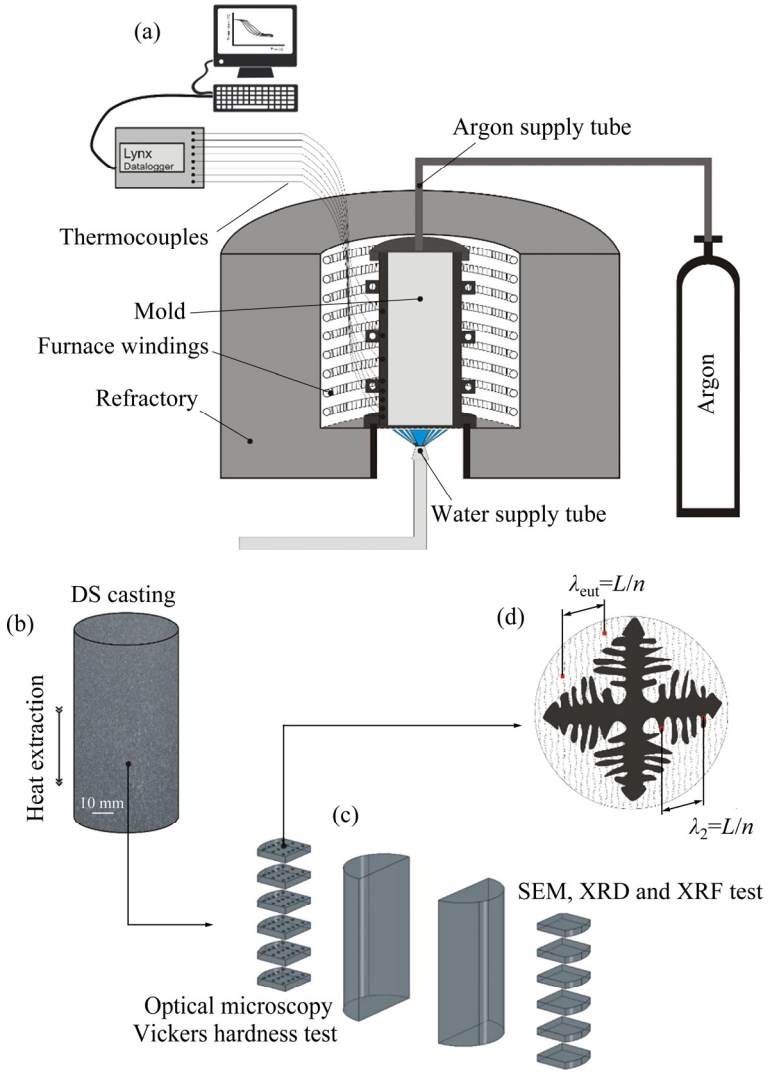

Fig. 1 Schematics of directional solidification (DS) apparatus (a), DS casting (b), representation of samples extracted along length of DS casting for further microstructure characterization and hardness tests (c) and representative scheme of technique used to quantify secondary dendritic arm (λ_2) and eutectic fiber (λ_{eut}) spacings (d)

3 Results and discussion

3.1 Solidification paths, microstructural phases and growth and cooling rates along length of DS castings

The pseudo binary Zn−1wt.%Mg−0.5wt.%Mn and Zn−1wt.%Mg−0.5wt.%Ca partial diagrams of Fig. 2(a) were calculated by the Thermo-Calc software, using the SSOL6 database, where the Zn−1wt.%Mg−0.5wt.%Mn (called Zn−1Mg−0.5Mn) and Zn−1wt.%Mg−0.5wt.%Ca (called Zn−1Mg−0.5Ca) alloys examined in the present study are indicated by vertical dotted lines. Based on the isopleths (Figs. 2(a) and (b)), the average compositions of the alloys were located, and from this, the transformation temperatures were obtained. The temperatures at which the cooling rates were determined are: η-Zn liquidus ($T_{L(\eta\text{-Zn})}$) and eutectic (T_{eut}) for the Zn−1Mg−0.5Mn alloy; η-Zn liquidus ($T_{L(\eta\text{-Zn})}$) and eutectic (T_{eut}) for the Zn−1Mg−0.5Ca alloy and additionally, $T_{CaZn_{13}}$ due to the growth of primary crystals of the $CaZn_{13}$ phase. The binary systems Zn−Mn [22,23] and Zn−Ca [24] present eutectic reactions for solute contents below 1 wt.%. In the Zn−Mn system this invariant reaction $L\rightarrow Zn+MnZn_9$ occurs at 413.2 °C for a content of Mn about 0.92 wt.%. The $MnZn_9$ phase has a density of ρ=7.09 g/cm^3, and an average Mn content of 8.53 wt.%; its Pearson symbol is *hP*2 and the space group is *P*63/*mmc* [20]. For the Zn−Ca system, the eutectic reaction $L\rightarrow Zn+CaZn_{13}$ occurs at 419.5 °C

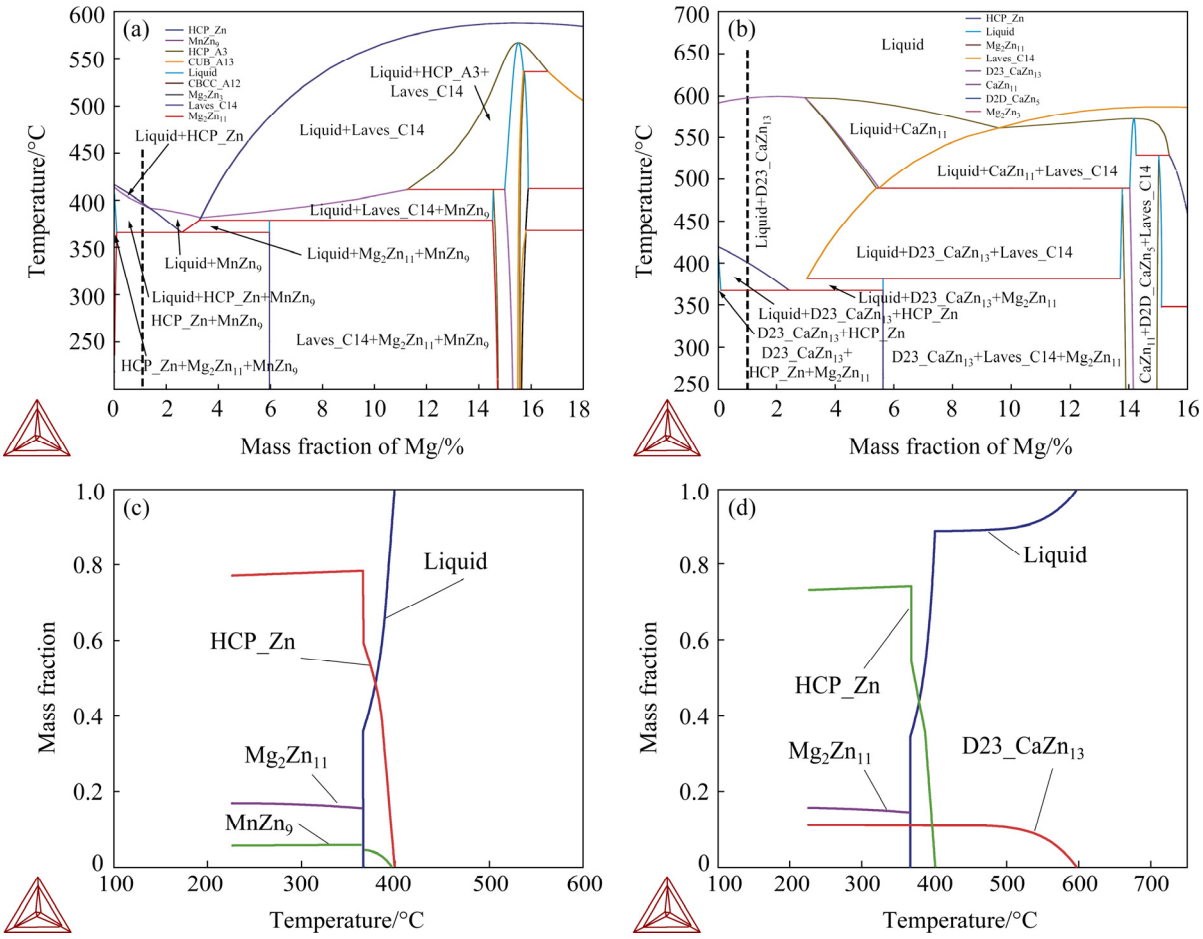

Fig. 2 Partial Zn−0.5(Mn, Ca)−*x*Mg pseudo binary phase diagrams (vertical dotted lines indicate alloys compositions examined in the present investigation) (a, b) and equilibrium phase fractions of Zn−1Mg−0.5Mn (c) and Zn−1Mg−0.5Ca (d) alloys as function of temperature, computed using SSOL6 database of Thermo-Calc software

and at 0.0032 wt.% Ca. The $CaZn_{13}$ phase is lighter than Zn, presenting ρ=6.47 g/cm^3 (ρ_{Zn}=7.14 g/cm^3), having a Ca content of about 4.5 wt.%; Pearson symbol is *cF*112 and the space group is $Fm\bar{3}c$ [25]. Figures 2(c) and (d) show the phases in equilibrium at a constant concentration, and predict the molar amount of all phases, with significant amounts of $MnZn_9$ and $CaZn_{13}$ phases. Therefore, these graphs are also proved to be suitable for the analyses of Scheil−Gulliver simulation. These curves show the solidification evolution in equilibrium conditions and corroborate the first analyses from the equilibrium phase diagram.

Figure 3 shows Scheil−Gulliver simulations and the corresponding experimental validation for both examined alloys. It allows the prediction of the growth sequence of each phase from the liquid (solidification path). In the Zn−1Mg−0.5Mn alloy (Fig. 3(a)) at 400 °C the η-Zn phase started to grow as the primary phase; shortly after at 396.6 °C the $MnZn_9$ phase grew from the liquid (concomitantly with the Zn phase); at 366.5 °C, a 38% eutectic fraction was obtained. For the Zn−1Mg−0.5Ca alloy (Fig. 3(b)), the primary phase started to grow at about 600 °C, i.e. the $CaZn_{13}$ phase was observed to occur first, with a molar fraction of 11% both under and out equilibrium conditions; then at 400 °C the η-Zn phase started to grow, and at 367 °C all the solute-enriched liquid will give rise to a 37% eutectic fraction. Figures 3(c) and (d) were obtained through slow cooling from the melt, with 300 g of alloy, and the cooling rate at each stage of solidification was indicated by the light gray arrows. The microstructures in Figs. 3(c) and (d) show the constituent phases of alloys. These cooling curves figured out experimentally the onset temperatures of transformation and corroborated

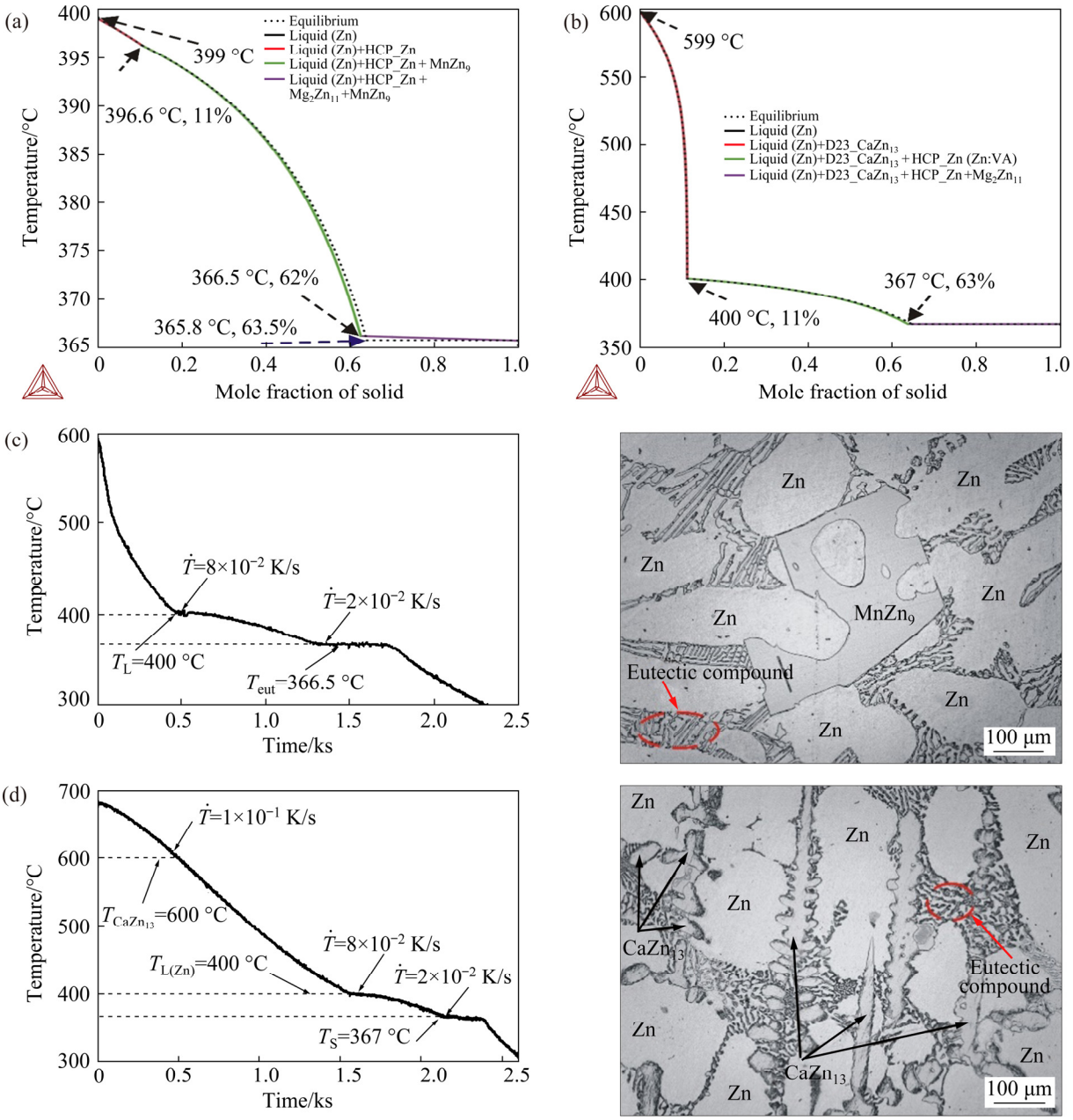

Fig. 3 Solidification paths of Zn−1Mg−0.5Mn (a) and Zn−1Mg−0.5Ca (b) alloys simulated by Thermo-Calc software based on non-equilibrium Scheil–Gulliver model (continuous line) and considering equilibrium conditions (dotted line) showing precipitation of phases during solidification, and experimental cooling curves under slow cooling rate and respective microstructural morphology of Zn−1Mg−0.5Mn (c) and Zn−1Mg−0.5Ca (d) alloys

those predicted by the Scheil−Gulliver simulations. These onset temperatures of transformation were used in the experimental calculation of cooling rates, as shown in Fig. 4.

The cooling curves of Figs. 4(a) and (b) were recorded using a data logger instrumented by K-type thermocouples. Plots of thermocoples location along the length of the casting (P) as a function of time of passage (t) of the liquidus (L) and eutectic (E) isotherms by each thermocouple, yield expression of the form: $P(t)=axt^b$, where a and b are constants. The derivatives of these functions with respect to time gave values for the growth rates V_L and V_{eut}, respectively. Figures 4(c) and (d) show the experimental values of growth rate (V) for both examined alloys together with the fitted evolutions.

The experimental cooling curves also allowed the determination of the evolution of cooling rates along the entire DS castings (Figs. 4(e) and (f)).

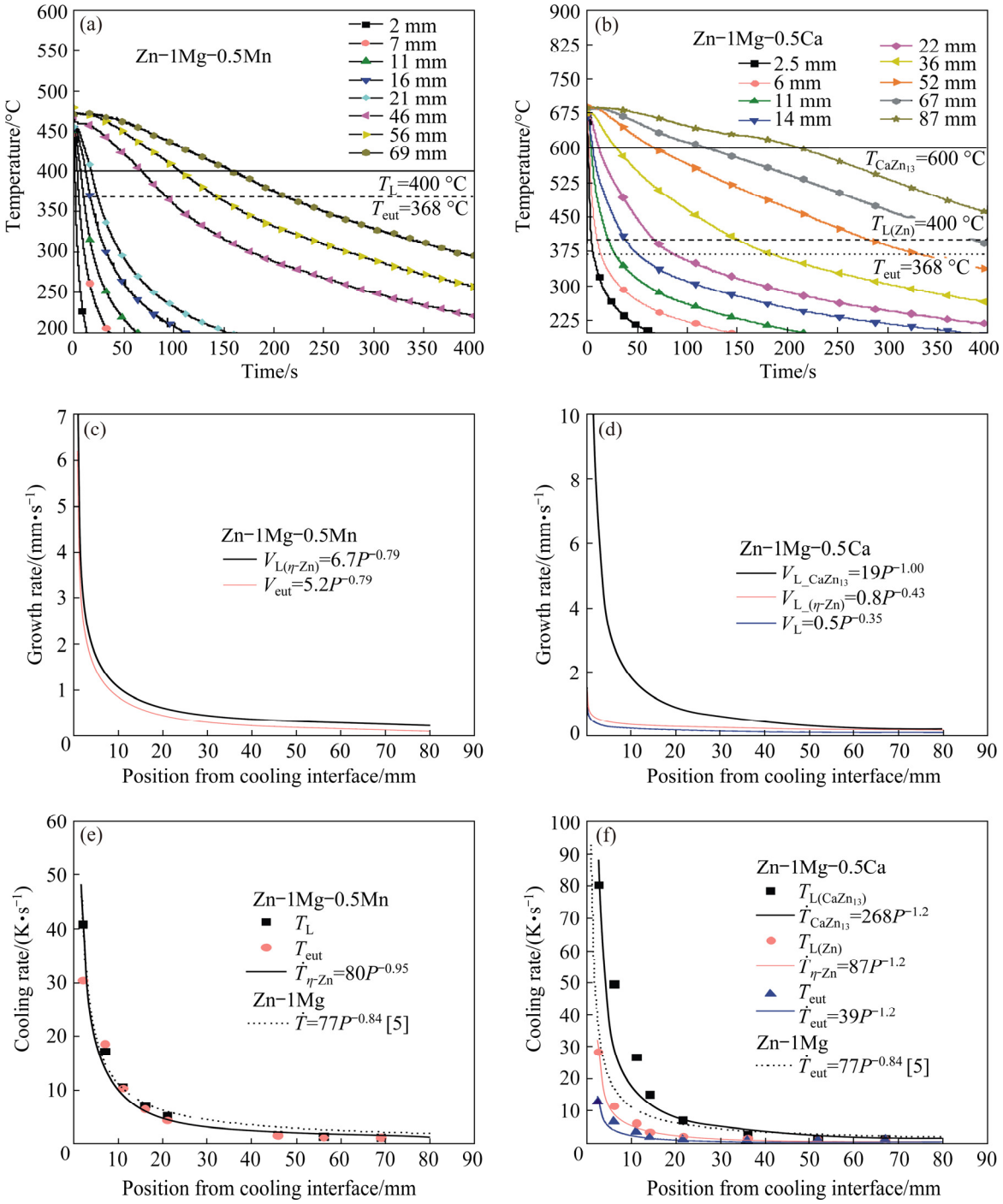

Fig. 4 Experimental cooling curves obtained from different thermocouple positions along length of DS castings of Zn−1Mg−0.5Mn (a) and Zn−1Mg−0.5Ca (b) alloys, growth rates of Zn−1Mg−0.5Mn (c) and Zn−1Mg−0.5Ca (d) alloys, and cooling rates of Zn−1Mg−0.5Mn (e) and Zn−1Mg−0.5Ca (f) alloy as function of position from cooling interface

The time of passage of the transformation isotherms was determined by the crossing and intersection between each cooling curve and the isotherms indicated in Figs. 4(a) and (b). A set of scatter temperatures within a range of 30 °C above and below of the transformation isotherms were fitted by a second degree polynomial function, $T=f(t)$. The cooling rate ($\dot{T}$) was obtained through the derivative of this function with respect to t, where t is the advance time of the transformation isotherm. The set of pairs $\dot{T}$ and position of the thermocouple (P) was used to establish fitted functions $\dot{T}=f(P)$. Considering the transformation isotherm of the η-Zn phase as representative of higher volumetric

fraction (Fig. 2) for both alloys, it can be seen that the occurrence of a quite expressive range of cooling rates varies from about 40 K/s for positions close to the cooled surface to less than 1 K/s near the top of the DS castings. Such significant range of cooling rates in a single casting experiment is expected to be associated with the corresponding expressive variation in the length scale of representative phases of the microstructure along the entire DS castings.

The advancement of the $T_{L(\eta\text{-Zn})}$ liquidus isotherm will be considered as a standard in a comparative analysis between the two studied alloys. The addition of Ca decreased the mean cooling rate values as compared to the cooling rate profile of the Zn−1Mg alloy [5], also in Figs. 4(e) and (f) for comparison purposes. This could be caused by differences in the alloy thermophysical properties induced by the addition of Ca, particularly in the thermal and volumetric contraction accompanying solidification, which will be reflected in the alloy/mold heat transfer coefficient (h). A decrease in h will be accompanied by a corresponding decrease in the cooling rate profile [26]. However, the determination of h is beyond the scope of the present investigation. In contrast, the addition of Mn seems to have no influence on this parameter. In the alloy containing Ca, the primary growth of the $CaZn_{13}$ phase gave rise to a first mushy zone (MZ), with a solidification interval of 200 °C. This first MZ changed the heat flow mode of the liquid to the environment, and also changed the time of latent heat release from the η-Zn phase. This change in the behavior of the heat flow may be related to the influence of the viscosity of the liquid on the velocity of heat extraction by conduction along the dendritic channels (Fig. 3(d)) of the $CaZn_{13}$ phase [27]. After the beginning growth of the η-Zn phase, a dendritic coherence was achieved and a solid fixed network was formed (as will be seen later), causing variation in the cooling rate profiles for the three analyzed isotherms.

The effect of the addition of Ca to the Zn−Mg system allowed a more detailed analysis to be carried out on the influence of composition and thermal solidification parameters on the final arrangement of the microstructure of the Zn−1Mg−0.5Ca alloy. According to Figs. 2(b) and 3(b), such alloy has a solidification interval of about 240 °C. The solutes Ca and Mg are not soluble in the η-Zn phase [28], and both are lighter than the solvent (Zn). The densities of the Mg, Ca and Zn are respectively 1.74, 1.54 and 7.10 g/cm^3 [28]. When the molten alloy during cooling reaches a temperature of 600 °C, each Ca atom will react with others 13 Zn atoms and nucleation of a $CaZn_{13}$ phase embryo will occur. As observed by VIDA et al [5] for DS Zn−Mg alloys, direct macrosegregation of Mg occurs along the length of the present alloy casting, and such solute movement can also occur with Ca, by the same principles. Such movement of solute will give rise to a supercooled liquid ahead the $CaZn_{13}$ isotherm, which will allow the growth of the Ca-bearing phase. These premises have allowed a scheme to predict the formation of the microstructural arrangement of this alloy to be drawn.

Figure 5 was developed based on the aforementioned premises, showing four instants of time resulting from the solidification of the Zn−1Mg−0.5Ca alloy: 0, 10, 100, and 500 s. Each frame presents a prediction of what is supposed to happen and its effect on the final arrangement of the microstructure for that condition. These predictions can be corroborated or confronted ahead in the discussion to follow, although for now they are important to outline how the concomitant growth of two primary phases, $CaZn_{13}$ and η-Zn, can occur. For t=0 s it is possible to observe the tendency of the solutes to float (red and white arrows), this upward movement can induce thermosolutal convection in the liquid (black arrow). For t=10 s the $CaZn_{13}$ isotherm is at 20 mm from the cooling interface, and the eutectic isotherm has already reached a position at about 5 mm from the bottom of the DS casting; the small particles represent the primary $CaZn_{13}$ phase, the dendrites (black) represent the η-Zn phase and the gray background represents the eutectic compound. After 100 s of the start of solidification, the $CaZn_{13}$ isotherm advanced 60 mm, and the first 20 mm of the DS casting was already solid; from this point on, there were conditions for the growth of the $CaZn_{13}$ phase with a dendritic equiaxed morphology. Finally, after 500 s it is possible to have a complete overview of the microstructural result of the unsteady state solidification of the Zn−1Mg−0.5Ca alloy.

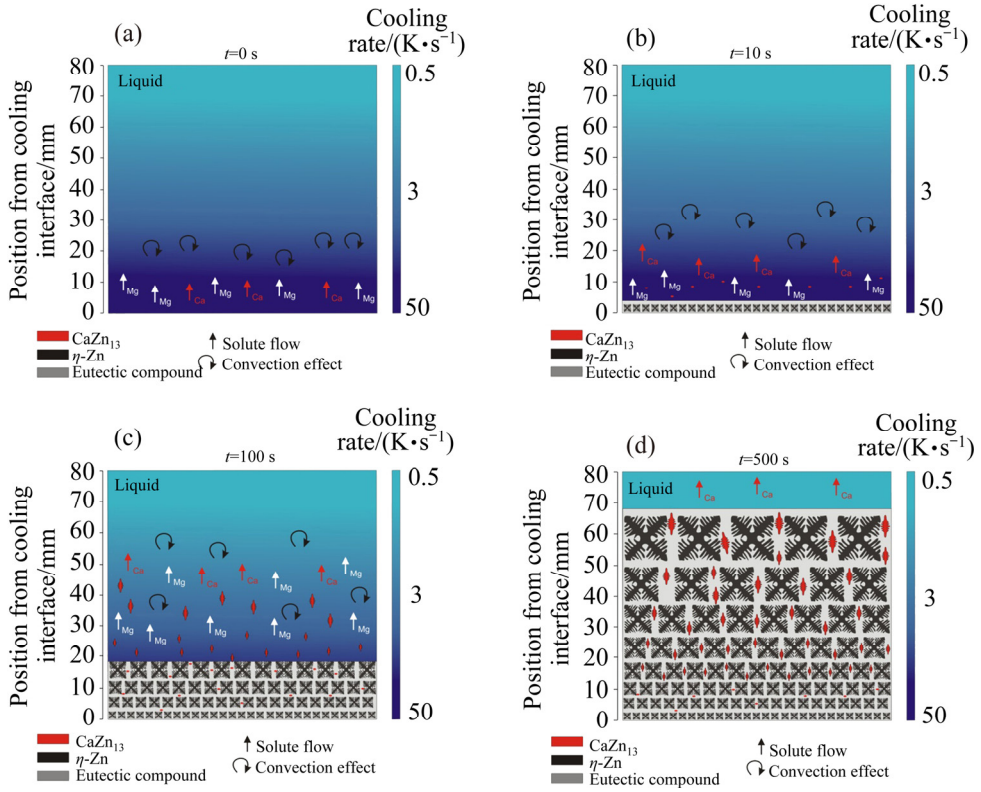

Fig. 5 Schematic prevision of growth of microstructural arrangement of Zn−1Mg−0.5Ca alloy along upward directional solidification process: (a) t=0 s; (b) t=10 s; (c) t=100 s; (d) t=500 s

3.2 Phases morphologies, microstructural spacings and growth laws

Figure 6 shows the experimental microstructural arrangements of the two analyzed alloys. An essentially dendritic morphology was shown to characterize the η-Zn phase (matrix) along the length of both alloys castings. The $MnZn_9$ and $CaZn_{13}$ phases were observed in the respective alloys, and the eutectic mixture (in the interdendritic regions) completed the microstructural arrangement. In a previous work [5] with a binary Zn−1Mg alloy, the growth of equiaxed grains was observed to occur along the entire range of experimental cooling rates analyzed, with a microstructure composed essentially of a Zn-rich (η-Zn phase) dendritic matrix plus a complex eutectic mixture (stable $Zn+Mg_2Zn_{11}$ and metastable $Zn+MgZn_2$). The variation in both microstructural morphology and length scale is associated with the cooling rate range varying between 45 and 0.2 K/s [5].

The addition of Mn to the Zn−1Mg alloy generated microstructures with a more refined dendritic morphology as compared to that of the binary alloy [5]. Zn_2Mg particles act as potent heterogeneous nucleation sites in Zn alloys [29]. However, BEDNARCZYK et al [30] have shown that among the solutes Cu, Ag and Mn, the latter acts as the most efficient grain refiner of Zn alloys, providing increased mechanical strength without considerable loss of ductility. The Zn−1Mg−0.5Mn alloy casting (Fig. 6(a_3)) with P=5 mm presents thin Zn dendrites with high incidence of secondary arms; the sample with P=70 mm shows that the morphology of the primary dendritic trunk follows the same morphological aspect of that observed in the previous study with the Zn−1Mg alloy [5], but with greater refinement of secondary arms. The $MnZn_9$ particles have an idiomorphic morphology and are distributed throughout the interdendritic branches.

Figure 2(b) showed that the phase diagram of the Zn−1Mg−0.5Ca alloy is quite distinct from that of the binary Zn−Mg alloy system [5]. Figure 3(b) and (d) indicated that, for the Zn−1Mg−0.5Ca alloy, the $CaZn_{13}$ phase would grow first and reach a mole fraction of about 11%. However, the micrographs in Figs. 6(b_1−b_3) showed a microstructural arrangement that depends on the magnitude of the cooling rate, which is different from that shown in

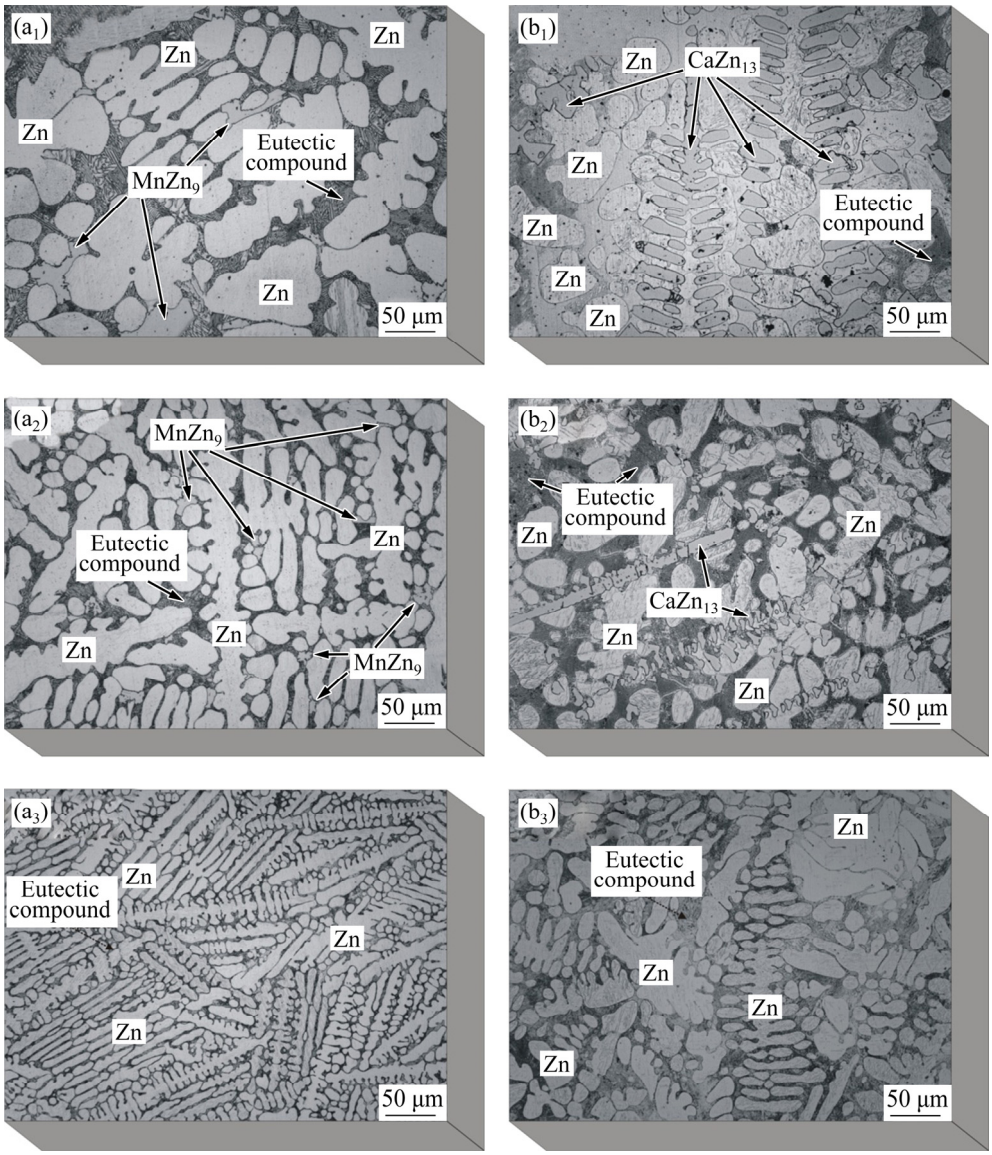

Fig. 6 Typical optical microstructures Zn−1Mg−0.5Mn (a_1−a_3) and Zn−1Mg−0.5Ca (b_1−b_3) alloys at three different positions (P) from cooled bottom of DS casting: (a_1, b_1) P=70 mm; (a_2, b_2) P=30 mm; (a_3, b_3) P=5 mm

Fig. 3(d) (sample solidified under a low cooling rate). Stable growth of the Ca-rich phase was observed to occur only for cooling rates ($\dot{T}_{\text{isotherm }\eta\text{-Zn}}$) below 1.8 K/s. For higher cooling rates the $CaZn_{13}$ phase grew with orthogonal dendritic morphology (growth where the secondary branches are orthogonal to the primary trunks) and aligned with the direction of heat extraction.

The addition of either Mn or Ca modified the morphology of the eutectic mixture present in the interdendritic regions, as shown in Fig. 7. A recent research [14] has shown that in hypoeutectic Zn−Mg alloys, the morphology of the eutectic mixture is composed of regular lamellae, degenerate lamellae and spiral lamellae. VIDA et al [14] classified the lamellar morphology into two categories: coarse lamella and refined lamella. In the Zn−1Mg−0.5Mn alloy, the addition of Mn prevented the formation of spiral lamellae. According to FULLMAN and WOOD [31], for this type of morphology to be able to grow, one or both of the phases should have anisotropic growth rates, so that the alpha (α) phase grows faster than the beta (β) phase in one direction or more slowly in other. The addition of Ca to the Zn−1Mg alloy modified the morphology of the lamellar eutectic to rod-like eutectic, in the presence of a minor fraction of lamellar morphology. However, different lamellae were observed to occur as compared to those reported for binary Zn−1Mg alloys. In this

case, the lamellar morphology was preferably observed at the edges of the η-Zn phase (Figs. 7(b_1) and (b_2)).

Figure 8(a) shows experimental growth laws relating the secondary dendritic arm spacing (λ_2) to cooling rate ($\dot{T}_{\eta\text{-Zn}}$). This plot has been figured out from the experimental λ_2 results measured along the DS Zn−1Mg−0.5Mn and Zn−1Mg−0.5Ca alloy castings. Power functions with an exponent of −1/3 characterize the evolution of λ_2 with $\dot{T}_{\eta\text{-Zn}}$. Recent studies on equiaxed directional solidification of hypoeutectic Zn−Mg [5,14] alloys have reported this same exponent, and these results are also inserted in Fig. 8(a) for comparison purposes. This exponent also agrees with those reported for secondary dendritic growth during transient directional solidification of Al and Zn-based ternary alloys [32−34]. Figure 8(b) shows the experimental scatters and growth laws relating eutectic spacings (λ_{eut}) to $\dot{T}$ for both experimentally examined Zn-

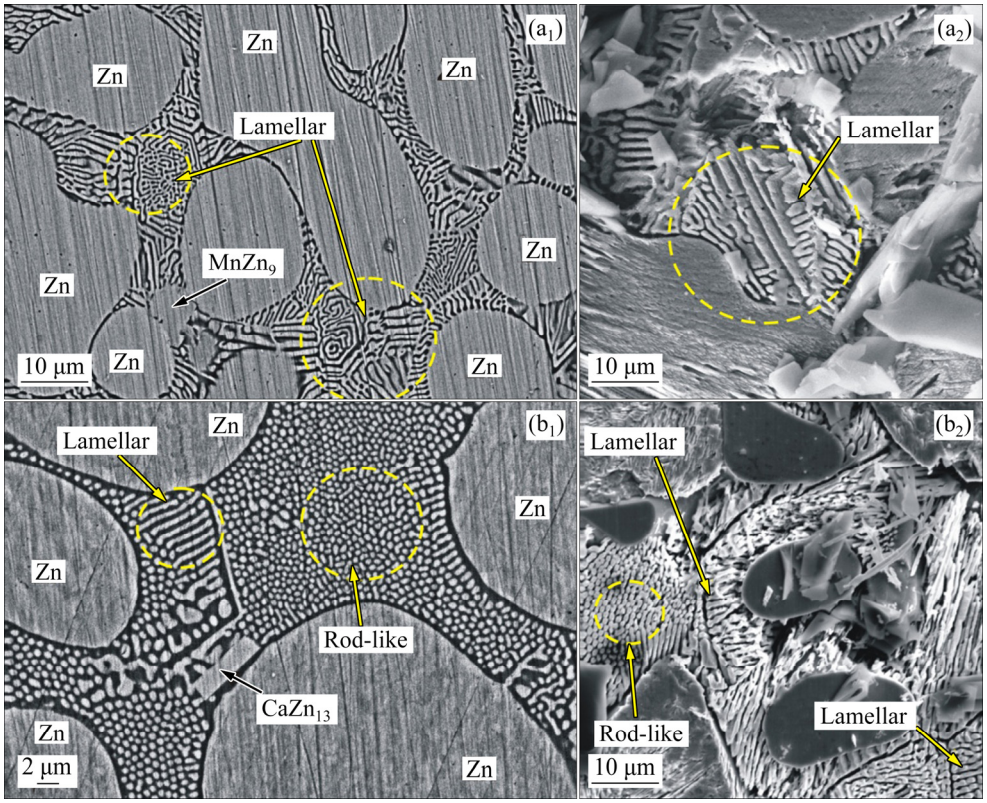

Fig. 7 SEM-BSE images of eutectic mixture for samples with P=30 mm: (a_1, a_2) Zn−1Mg−0.5Mn alloy, in which arrows indicate regions of lamellar morphology; (b_1, b_2) Zn−1Mg−0.5Ca alloy, in which arrows indicate regions with rod-like and lamellar morphologies

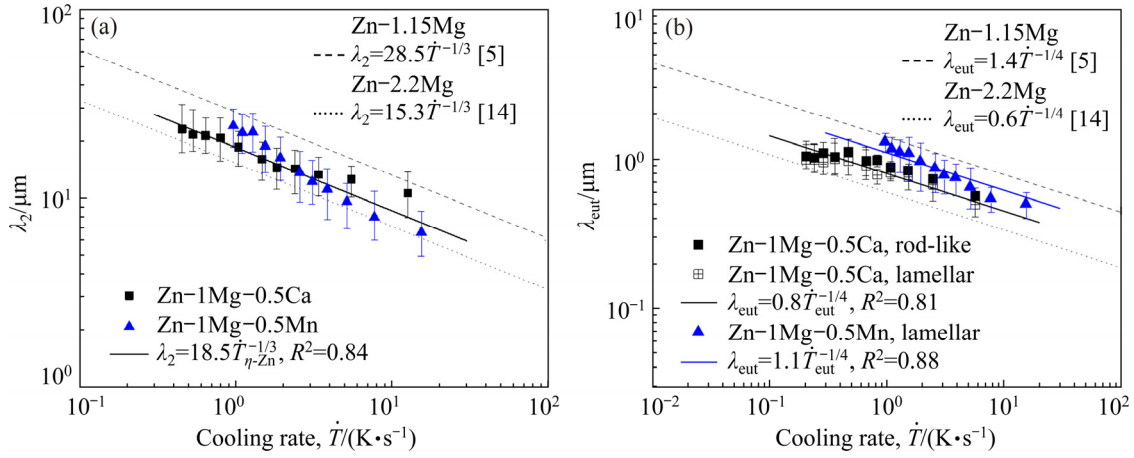

Fig. 8 Secondary dendritic arm spacing as function of solidification cooling rate, λ_2 vs $\dot{T}$ (a), and eutectic spacing as function of solidification cooling rate, λ_{eut} vs $\dot{T}$ (b)

based alloys. It can be seen that a −1/4 exponent characterizes the present experimental power laws.

The alloy with Ca solidified under an average profile of cooling rate lower than that of the binary alloy Zn−1Mg. However, Fig. 8 depicted a smaller dispersion in the values of the microstructural parameters standardized by λ_2 and λ_{eut}, and corroborated by the growth laws. The liquid in contact with the solid/liquid interface (S/L) has become richer in solute due to solute rejection in front of this interface. Mg, Mn or Ca solutes have no solubility in the η-Zn phase, and regardless of the upward flow of the solutes (Ca and Mg) or their accumulation just in front of the S/L (Mn) interface, there will be a local composition that will differ from the concentration of the open liquid. This gradient of solute concentration will cause the formation of a thermal gradient in the liquid, and in the regions close to the S/L interface the formation of a constitutional supercooling (CS) will be observed. The CS level has a strong influence on the morphology of the S/L interface and is directly proportional to the C_0 (C_0 is the alloy nominal composition) level. Several studies have shown the influence of CS on the rate of nucleation and microstructural refining [35−38]. VIDA et al [14] proposed that a growth law of type $\lambda_2=15.3\dot{T}^{-1/3}$ would be more adequate than the model proposed by BOUCHARD and KIRKALDY [35] for predicting the growth of secondary dendritic spacing of hypoeutectic Zn−Mg alloys solidified in steady state and unsteady state conditions. The same was obtained for the evolution of the growth of eutectic spacings [14], as shown by the dotted curves in Fig. 8(b).

For Zn−Mg based alloys subjected to the directional solidification technique used in the present study, the growth from the melt progresses vertically upwards, and since Zn is much denser than Mg, Mg can float (by gravity effects) ahead of the solidification front, thus enriching the molten alloy with Mg. This is typical of Zn−Mg alloys, as reported by VIDA et al [5] in a study on directional solidification of Zn−(0.3−1.2)wt.%Mg alloys, for which normal macrosegregation Mg profiles were reported to occur. Figure 9(a) shows the experimental solute concentration profiles determined along the length of the Zn−1Mg−0.5Mn DS casting. It can be seen that the experimental solute profiles for Mn and Mg are essentially constants along the entire casting. At this point, the Mg concentration profile along the entire casting behaved differently from that observed for binary Zn−(0.3−1.2)wt.%Mg alloys [5]. The presence of Mn seems to have altered the rejection and redistribution mechanism of Mg ahead the solid/liquid interface. The growth of the $MnZn_9$ phase appears to have created a type of barrier that prevented the Mg-rich liquid (less dense) from floating upwards.

In contrast, a rising Ca profile can be observed characterizing the occurrence of normal macrosegregation in Fig. 9(b). According to the Zn−Ca binary phase diagram [24], Ca is not soluble in the η-Zn phase. According to Figs. 2 and 3 for the Zn−1Mg−0.5Ca alloy, the $CaZn_{13}$ phase grows, which is lighter than the open liquid and has a wide solidification interval, factors that may have contributed to upward displacement of this phase. Therefore, the lower Ca content for regions closer to the cooled bottom of the casting can be related to two features. Firstly, these regions are associated with high cooling rates, which seem to suppress the formation of the Ca-bearing phase (fact corroborated by the presence of Ca dissolved in the eutectic mixture). Secondly, the Ca-bearing phase is lighter than the open liquid, and thus it can float. For $\dot{T}_{\eta\text{-Zn}}<1.8$ K/s, there are conditions for the growth of the $CaZn_{13}$ phase, and from this point the fraction of this phase becomes greater, which is associated with the increasing Ca profile of Fig. 9(b).

Figure 9(c) and (d) show the results of X-ray diffraction (XRD) analysis. The Zn−Mg system is known to exhibit two competitive types of eutectic mixtures. In this way, three phases common to the two analyzed alloys were identified: η-Zn, and the intermetallic compounds $Zn_{11}Mg_2$ and Zn_2Mg (present in the eutectic mixture). The $MnZn_9$ phase has been identified along the entire range of experimental cooling rates of the DS Zn−1Mg−0.5Mn alloy casting. In this case, the peaks with 2θ angles of 38.9°, 43.01° and 82.15°, common to the three tested samples, indicate the occurrence of the Mn-bearing phase also for regions with higher cooling rates. In the Zn−1Mg−0.5Ca alloy casting, two Ca-bearing phases have been identified, i.e. the $CaZn_{11}$ and the $CaZn_{13}$ phases. According to the isopleth of Fig. 2(b), the $CaZn_{11}$ phase should not occur for this level of Ca content. Figure 9(d)

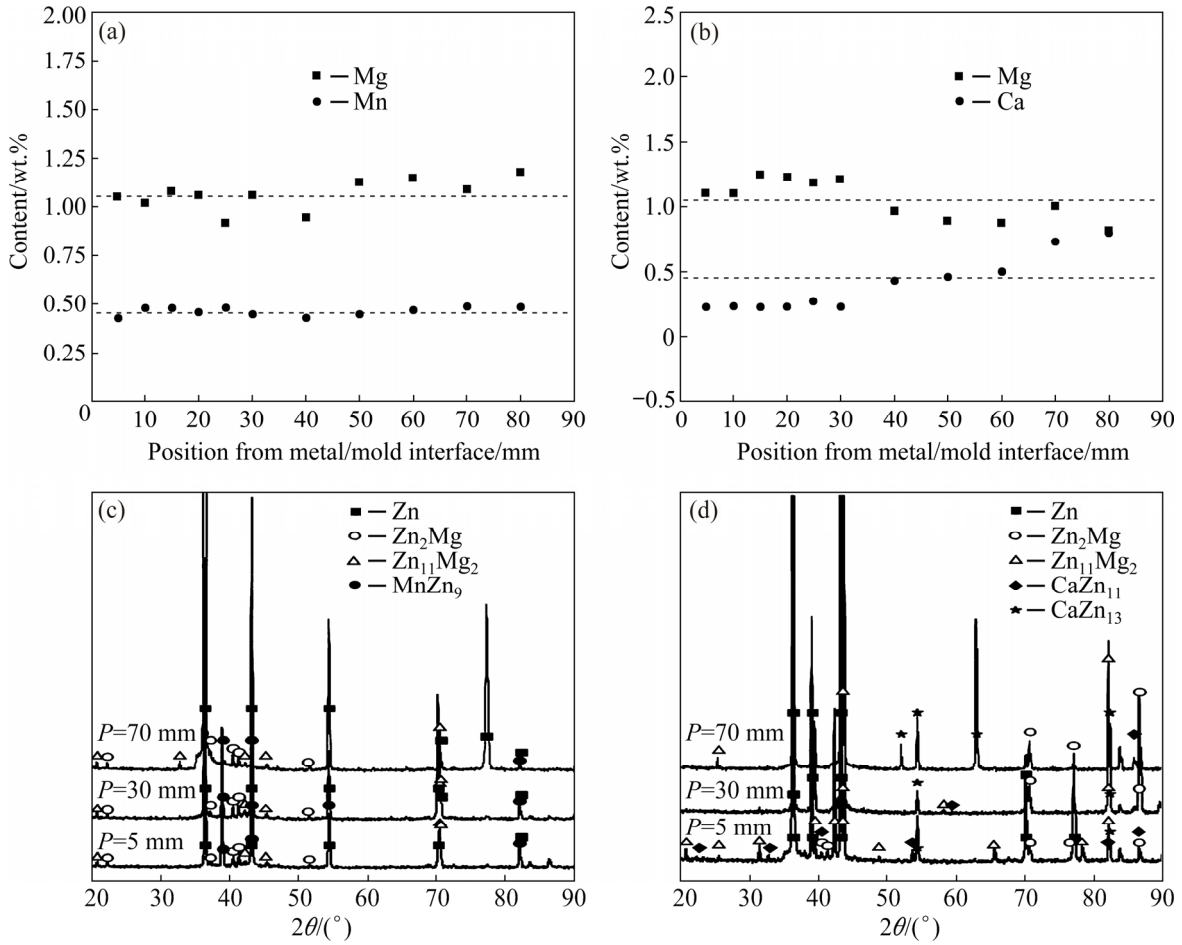

Fig. 9 Solute content profiles along length of DS castings (a, b) and XRD patterns (c, d) at three different positions (P) in DS castings referring to different solidification cooling rates: (a, c) Zn−1Mg−0.5Mn; (b, d) Zn−1Mg−0.5Ca

shows that this phase occurs mainly in the sample with P=5 mm ($\dot{T}_{\text{isotherm }\eta\text{-Zn}}$ >10 K/s), indicating that the magnitude of the cooling rate under non-equilibrium solidification conditions affects the growth of the phases, forming the microstructure of these alloys. LI et al [39] analyzed a Zn−1Mg−1Ca alloy in conditions such as cast and hot-rolled, and they have not observed the presence of $CaZn_{11}$ in these conditions. Other studies that examined the addition of Ca to hypoeutectic Zn−Mg alloys, also do not report the presence of $CaZn_{11}$ [40,41].

Figures 10(a_1−a_3) and (b_1−b_3) show the results of SEM/energy dispersive X-ray spectroscopy (EDS) analysis with the mass fraction of each of the phases at different positions along the length of the Zn−1Mg−0.5Mn and Zn−1Mg−0.5Ca alloys castings, respectively. Next to each image there is a table with the punctual results of the analyses with the mass fraction of the elements. The analyses were performed at different positions in each alloy casting, seeking to verify the influence of the cooling rate on the formed phases. The alloy containing Mn appears in both the η-Zn matrix and the Zn phase of the eutectic mixture with an average Mn content of about 0.3 wt.%, suggesting the presence of a supersaturated metastable η-Zn phase. The dark phase (of lamellar morphology) present in the eutectic region of the microstructure is formed by Mg-bearing phases ($Zn_{11}Mg_2$ and Zn_2Mg). It is worth mentioning that the EDS analysis presents a certain discrepancy when measuring thin phases, mainly with thicknesses smaller than that of the EDS beam (the X-ray beam of the equipment used has a diameter of about 1 μm). Thus, for the more refined regions of the samples, the analysis may not include the values provided in the literature for the composition of each phase. In this sense, this reinforces the need for X-ray diffraction (XRD) analyses, which were carried out to give more reliability to the results.

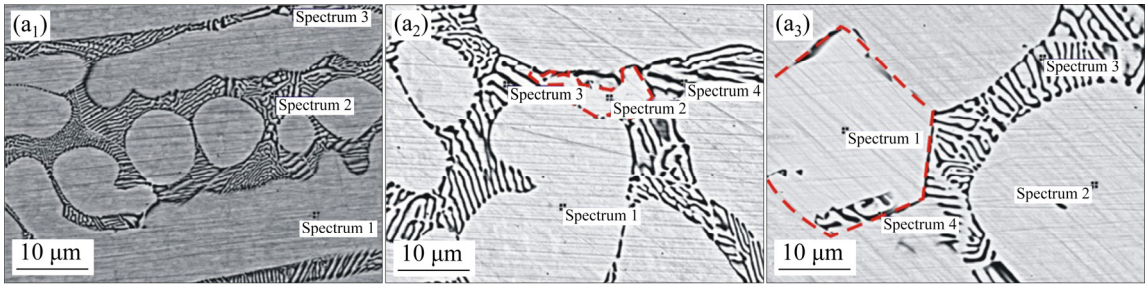

Spectrum No.	Mass fraction/%		
	Mg	Mn	Zn
1	0	0	100.00
2	4.61	0.61	94.78
3	5.63	0.63	93.74

Spectrum No.	Mass fraction/%		
	Mg	Mn	Zn
1	0	0.29	99.71
2	0.88	4.95	94.17
3	1.33	0.27	98.41
4	8.52	0.34	91.14

Spectrum No.	Mass fraction/%		
	Mg	Mn	Zn
1	1.31	5.05	93.64
2	0	0.34	99.66
3	0.49	0.26	99.25
4	11.46	2.25	86.29

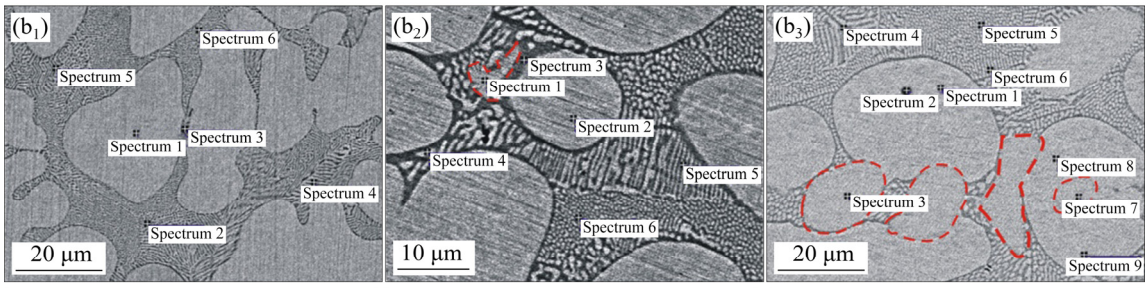

Spectrum No.	Mass fraction/%		
	Mg	Ca	Zn
1	0	0	100.00
2	3.12	0	96.88
3	1.69	0	98.31
4	2.24	0	97.76
5	7.09	0	92.91
6	2.83	0	97.17

Spectrum No.	Mass fraction/%		
	Mg	Ca	Zn
1	0	3.21	96.79
2	0	0	100.00
3	7.00	0	93.00
4	1.59	0	98.41
5	4.21	0.17	95.62
6	4.39	0	95.61

Spectrum No.	Mass fraction/%		
	Mg	Ca	Zn
1	0	0	100.00
2	0	0	100.00
3	0	4.66	95.34
4	5.89	0	94.11
5	2.79	0	97.21
6	4.28	0	95.72
7	0	4.85	95.15
8	0	0	100.00
9	0	0	100.00

Fig. 10 SEM/EDS results of areas inside dendritic and interdendritic regions for different positions in Zn−1Mg−0.5Mn (a_1−a_3) and Zn−1Mg−0.5Ca (b_1−b_3) alloy castings: (a_1, b_1) P=5 mm; (a_2, b_2) P=30 mm; (a_3, b_3) P=70 mm

As shown in Fig. 6(b_1) for the sample with P=70 mm, the Ca-bearing phase could be better observed in samples solidified under $\dot{T}_{\text{isotherm }\eta\text{-Zn}} <$ 1.8 K/s. It can be seen in Fig. 9(d) that there was a higher incidence of 2θ peaks associated with the $CaZn_{13}$ phase, thus, it can be inferred that the phase with dendritic morphology dispersed in the η-Zn matrix is the $CaZn_{13}$ phase. Figures 10(b_1−b_3) also indicate the absence of Ca in the η-Zn phase, and some Ca solubility in the eutectic region [41].

3.3 Vickers microhardness

The addition of Mn and Ca to the Zn−1Mg alloy contributed to a substantial increase in Vickers hardness (HV) values as compared to the binary alloy, as shown in Fig. 11. The Zn−1Mg−0.5Mn alloy showed a behavior dependent on the length scale of the dendritic microstructure, following a classic Hall−Petch relationship, with higher Vickers hardness values associated with lower values of λ_2, and an average increase of 30% in the Vickers hardness values in relation to the binary alloy. The Zn−1Mg−0.5Ca alloy casting showed two different evolution profiles in Vickers hardness. An inflection point occurred in the sample with P=25 mm (with $\dot{T}_{CaZn_{13}}$ = 5.6 K/s and $\dot{T}_{\eta\text{-Zn}}$ = 1.8 K/s); λ_2=15.2 μm (or $\lambda_2^{-1/2}$=0.257 $\mu m^{-1/2}$), for which the lowest hardness value of 94 HV can be observed. The sample with P=5 mm and λ_2=7.9 μm (or $\lambda_2^{-1/2}$=0.354 $\mu m^{-1/2}$) presented a hardness of 105 HV, and the sample with P=80 mm and λ_2=24.1 μm (or $\lambda_2^{-1/2}$=0.203 $\mu m^{-1/2}$) a hardness of 125 HV.

The microstructural arrangement of the sample with P=5 mm is essentially constituted by a dendritic η-Zn matrix and the eutectic mixture (Fig. 6(b_1−b_3)). In this case, the increase in hardness as compared to that of the Zn−1Mg alloy is probably caused by (I) the greater refinement of the eutectic compound (Fig. 8(b)), as shown by the sample with P=5 mm for which $\lambda_{eut}^{-1/2}$ values of about 1.25, 1.41, 1.32 (rod-like)/ 1.41(lamellar) μm$^{-1/2}$, for the Zn−1Mg, Zn−1Mg−0.5Mn and Zn−1Mg−0.5Ca alloys, respectively, can be observed; (II) the presence of Ca-bearing phases and the modification of the eutectic morphology (variation from an essentially lamellar to a lamellar+rods morphology, see Figs. 7(b_1, b_2)) seem to have contributed to the higher Vickers hardness value as compared to the alloy containing Mn.

As aforementioned, the stable growth of the $CaZn_{13}$ phase could only occur for lower cooling rates ($\dot{T}_{\eta\text{-Zn}}$ <1.8 K/s); Fig. 9(b) showed a slight direct macrosegregation profile of Ca (from sample with P=30 mm) that increases progressively towards the top of the casting. Figures 6(b_1−b_3) and 7(b_1, b_2) showed the presence of this phase from this sample. This configuration indicates that the increase in hardness for progressively coarser dendritic microstructures is causally related to the stable growth and increasing fraction of the $CaZn_{13}$ phase towards the top of the casting. The $CaZn_{13}$ phase serves as an “anchor” to the movement of dislocations, thus providing the increase in hardness. This set of factors provided a linear increase in Vickers hardness up to a maximum of 125 HV, that is, an increase of about 90% in relation to that of the Zn−1Mg alloy.

The experimental results of Vickers hardness of the Zn−1Mg alloy casting were obtained following the same procedure used for the two alloys analyzed in the present study and described in the experimental procedure section. The experimental values are also plotted in Fig. 11, being essentially constant along the length of the DS casting at about 65 HV. In a previous work [5], it was reported that this alloy presented a normal (or direct) Mg macrosegregation profile, that is, increasing the Mg content from bottom to top of the DS casting, which has contributed to the increase in the eutectic fraction, and consequently in the fraction of Mg-bearing phases. A balance seems to have occurred from bottom to top of the DS casting, leading to an essential constant hardness, i.e. with the increase in both λ_2 and eutectic fraction. For lower λ_2, the lower reinforcing eutectic fraction is more homogeneously distributed throughout the interdendritic spacings of the microstructure, whereas with the increase in λ_2, hardness is kept in a similar value due to the increase in the fraction of the eutectic phase.

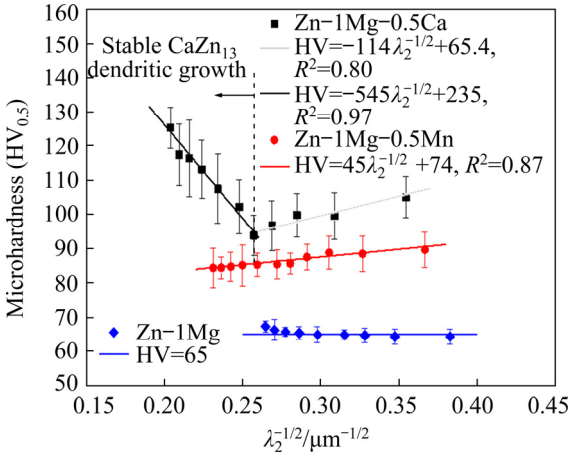

Fig. 11 Evolution of Vickers microhardness (HV) with square root of secondary dendritic spacings along length of DS alloy castings

The greater hardness observed for Ca-bearing alloys, is actually associated with the growth of the $CaZn_{13}$ phase during solidification of the Zn−1Mg−0.5Ca alloy. According to Fig. 2, it is the primary phase and represents a volumetric fraction of at least 10% of the microstructural arrangement. In contrast to the Mn-bearing alloy, the $MnZn_9$ phase represents less than 1% of the volumetric fraction of the microstructure (Fig. 2(b)). The difference between the microhardness values of these two alloys is at least 25%. The cooling rate also has an important influence on these final Vickers hardness values, since the scale of the final arrangement of the solidification morphology is directly linked to the level of cooling rate imposed during the solidification stage [29,42−44]. Figure 12 summarizes the average values obtained experimentally for the alloys (considering the Vickers indentation of the microstructural arrangement); for each phase of the microstructural arrangement (considering the Vickers indentation of only the area of the phase), for each eutectic mixture (considering the Vickers indentation of only the interdendritic area), and lastly the Vickers hardness of Zn available in literature [28].

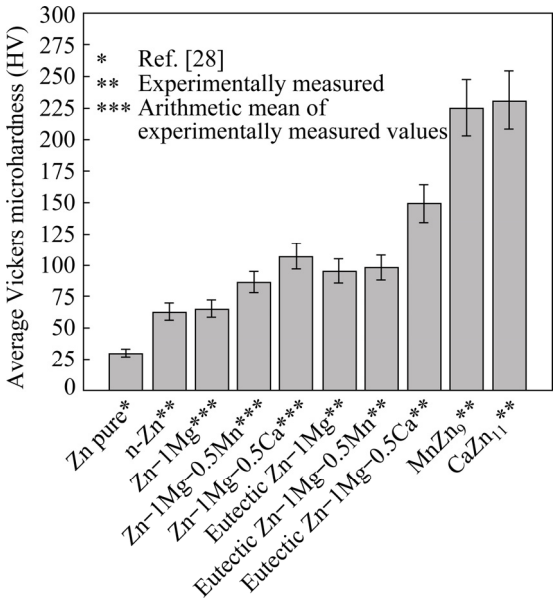

Fig. 12 Average Vickers microhardness for each phase or compound present in microstructural arrangement

4 Conclusions

(1) Three common phases were shown to form the microstructures of the Zn−Mg−(Ca, Mn) DS alloy castings: the Zn-rich dendritic matrix and the $Zn_{11}Mg_2$ and Zn_2Mg IMCs present in the eutectic mixture. Complementary, for the particular cases of Ca and Mn additions, two Ca-bearing phases ($CaZn_{11}$ and $CaZn_{13}$) and the $MnZn_9$ were also formed, respectively. These additions also promoted not only the refinement of both dendritic and eutectic phases, but also modify the morphology of the eutectic: Mn prevented the formation of spiral lamellae and Ca modified the lamellar eutectic into a rod-like eutectic.

(2) A normal Ca macrosegregation profile, that is, an increasing Ca profile (from about 0.25 up to 0.8 wt.% Ca) from the bottom to the top of the vertical Zn−1Mg−0.5Ca DS alloy casting was observed to occur. In contrast, the Mn and Mg solute profiles remained essentially constant along the length of the DS castings.

(3) Experimental growth laws were proposed relating the secondary dendritic arm spacing (λ_2: μm) and the eutectic interphase spacing (λ_{eut}: μm) to experimental cooling rates ($\dot{T}$: K/s): $\lambda_2=18.5\dot{T}_{\eta\text{-Zn}}^{-1/3}$ for both Zn−1Mg−0.5Ca and Zn−1Mg−0.5Mn alloys; $\lambda_{eut}=0.8\dot{T}_{eut}^{-1/4}$ for the Zn−1Mg−0.5Ca alloy and $\lambda_{eut}=1.1\dot{T}_{eut}^{-1/4}$ for the Zn−1Mg−0.5Mn alloy.

(4) The Mn and Ca additions to the Zn−1Mg alloy have proven to be effective in the increase in Vickers microhardness (HV) as compared to the binary alloy. Correlations between λ_2 and Vickers microhardness along the length of the DS castings permitted Hall−Petch type equations to be proposed, generally agreeing with the classical trend of higher Vickers microhardness associated with lower λ_2. An exception concerns the increase in Vickers microhardness for the Zn−1Mg−0.5Ca alloy as the dendrites get coarser ($\dot{T}$ <1.8 K/s) justified by the increase in the fraction of the $CaZn_{13}$ IMC towards the top of the casting.

Acknowledgments

The authors are grateful to FAPESP-São Paulo Research Foundation, Brazil (2014/50502-5 and 2017/16058-9), Capes-Coordenação de Aperfeiçoamento de Pessoal de Nível Superior, Brazil (Funding code 001) and CNPq-National Council for Scientific and Technological Development (406239/2018-5) for their financial support. The authors would like to thank the Brazilian Nanotechnology National Laboratory–LNNano for allowing us to use its facilities.

References

[1] KRIEG R, VIMALANANDAN A, ROHWERDER M. Corrosion of zinc and Zn−Mg alloys with varying microstructures and magnesium contents [J]. Journal of the Electrochemical Society, 2014, 161: C156−C161.

[2] MOSTAED E, SIKORA-JASINSKA M, MOSTAED A, LOFFREDO S, DEMIR A G, PREVITALI B, MANTOVANI D, BEANLAND R, VEDANI M. Novel Zn-based alloys for biodegradable stent applications: Design, development and in vitro degradation [J]. Journal of the Mechanical Behavior of Biomedical Materials, 2016, 60: 581−562.

[3] GONG H, WANG K, STRICH R, ZHOU J G. In vitro biodegradation behavior, mechanical properties, and cytotoxicity of biodegradable Zn−Mg alloy [J]. Journal of Biomedical Materials Research Part B: Applied Biomaterials, 2015, 103(8): 1632−1640.

[4] YAO C, WANG Z, TAY S L, ZHU T, GAO W. Effects of Mg on microstructure and corrosion properties of Zn−Mg alloy [J]. Journal of Alloys and Compounds, 2014, 602: 101−107.

[5] VIDA T A, FREITAS E S, BRITO C, CHEUNG N, ARENAS M A, CONDE A, DAMBORENEA J, GARCIA A. Thermal parameters and microstructural development in directionally solidified Zn-rich Zn−Mg alloys [J]. Metallurgical and Materials Transactions A, 2016, 47(6): 3052−3064.

[6] FERREIRA A F, CHRISÓSTIMO W B, SALES R C, GARÇÃO W J L, de PAULA SOUSA N. Effect of pouring

temperature on microstructure and microsegregation of as-cast aluminum alloy [J]. The International Journal of Advanced Manufacturing Technology, 2019, 104(1−4): 957−965.

[7] de SOUZA BAPTISTA L A, PARADELA K G, FERREIRA I L, GARCIA A, FERREIRA A F. Experimental study of the evolution of tertiary dendritic arms and microsegregation in directionally solidified Al−Si−Cu alloys castings [J]. Journal of Materials Research and Technology, 2019, 8(1): 1515−1521.

[8] SOARES T, CRUZ C, BARROS A, GARCIA A, CHEUNG N. Microstructure, growth morphologies, macrosegregation and microhardness in Bi−Sb thermal interface materials [J]. Advanced Engineering Materials, 2020, 22: 1901592.

[9] BÜYÜK U, ENGIN S, KAYA H, ÇADIRLI E, MARAŞLI N. Directionally solidified Al−Cu−Si−Fe quaternary eutectic alloys [J]. Physics of Metals and Metallography, 2020, 121(1): 78−83.

[10] XAVIER M G C, SOUZA T M G, CHEUNG N, GARCIA A, SPINELLI J E. Effects of cobalt and solidification cooling rate on intermetallic phases and tensile properties of a Cu−Zn−Fe containing Al−Si alloy [J]. The International Journal of Advanced Manufacturing Technology, 2020, 107(1): 717−730.

[11] COSTA T A, DIAS M, SILVA C, FREITAS E, SILVA A P, CHEUNG N, GARCIA A. Measurement and interrelation of length scale of dendritic microstructures, tensile properties and machinability of Al−9wt.%Si−(1wt.%Bi) alloys [J]. The International Journal of Advanced Manufacturing Technology, 2019, 105(1−4): 1391−1410.

[12] BOTELHO T M, AZEVEDO H M, MACHADO G H, BARBOSA C R, ROCHA F S, COSTA T A, ROCHA O L. Effect of solidification process parameters on dry sliding wear behavior of AlNiBi alloy [J]. Transactions of Nonferrous Metals Society of China, 2020, 30(3): 582−594.

[13] ÇADIRLI E, BÜYÜK U, ENGIN S, KAYA H. Effect of silicon content on microstructure, mechanical and electrical properties of the directionally solidified Al-based quaternary alloys [J]. Journal of Alloys and Compounds, 2017, 694: 471−479.

[14] VIDA T A, BRITO C, LIMA T S, SPINELLI J E, CHEUNG N, GARCIA A. Near-eutectic Zn−Mg alloys: Interrelations of solidification thermal parameters, microstructure length scale and tensile/corrosion properties [J]. Current Applied Physics, 2019, 19(5): 582−598.

[15] HERNÁNDEZ-ESCOBAR D, CHAMPAGNE S, YILMAZER H, DIKICI B, BOEHLERT C J, HERMAWAN H. Current status and perspectives of zinc-based absorbable alloys for biomedical applications [J]. Acta Biomaterialia, 2019, 97: 1−22.

[16] KURZ W, FISHER D J. Dendrite growth at the limit of stability: Tip radius and spacing [J]. Acta Metallurgica, 1981, 29(1): 11−20.

[17] TRIVEDI R. Interdendritic spacing: Part II. A comparison of theory and experiment [J]. Metallurgical and Materials Transactions A, 1984, 15(6): 977−982.

[18] HUNT J D, LU S. Numerical modeling of cellular/dendritic array growth: Spacing and structure predictions [J]. Metallurgical and Materials Transactions A, 1996, 27(3): 611−623.

[19] GÜNDÜZ M, ÇADIRLI E. Directional solidification of aluminium–copper alloys [J]. Materials Science and Engineering A, 2002, 327(2): 167−185.

[20] Inorganic crystal structure database, crystallographic information framework (CIF) files [EB/OL] [2020−08−9]. http://www.fizkarlsruhe.de/icsd.html.

[21] ASTM. E92-16 Standard test methods for Vickers hardness and Knoop hardness of metallic materials [S]. 2016.

[22] ZHANG L J, DU Y, XU H H, ZHAO J R. Thermodynamic description of the Mn−Si−Zn system [J]. Science China Technological Sciences, 2012, 55(2): 475−483.

[23] OKAMOTO H, TANNER L E. The Mn−Zn (manganese−zinc) system [J]. Bulletin of Alloy Phase Diagrams, 1990, 11(4): 377−384.

[24] OKAMOTO H. Ca−Zn (calcium−zinc) [J]. Journal of Phase Equilibria and Diffusion, 2013, 34(2): 171.

[25] ZHANG Y N, KEVORKOV D, BRIDIER F, MEDRAJ M. Experimental study of the Ca–Mg–Zn system using diffusion couples and key alloys [J]. Science and Technology of Advanced Materials, 2011, 12(2): 025003.

[26] QUARESMA J M V, SANTOS C A, GARCIA A. Correlation between unsteady-state solidification conditions, dendritic spacings and mechanical properties of Al−Cu alloys [J]. Metallurgical and Materials Transactions A, 2000, 31: 3167−3178.

[27] STEFANESCU D M. Science and engineering of casting solidification [M]. Heidelberg: Springer, 2015.

[28] NAYAR A. The metals databook [M]. New York: McGraw-Hill, 1997.

[29] LIU Z L, QIU D, WANG F, TAYLOR J A, ZHANG M X. Grain refinement of cast zinc through magnesium inoculation: Characterization and mechanism [J]. Materials Characterization, 2015, 106: 1−10.

[30] BEDNARCZYK W, WATROBA M, KAWALKO J, BALA P. Can zinc alloys be strengthened by grain refinement? A critical evaluation of the processing of low-alloyed binary zinc alloys using ECAP [J]. Materials Science and Engineering A, 2019, 748: 357−366.

[31] FULLMAN R L, WOOD D L. Origin of spiral eutectic structures [J]. Acta Metallurgica, 1954, 2(2): 188−193.

[32] KAKITANI R, CRUZ C B, LIMA T S, BRITO C, GARCIA A, CHEUNG N. Transient directional solidification of a eutectic Al−Si−Ni alloy: Macrostructure, microstructure, dendritic growth and hardness [J]. Materialia, 2019, 7: 100358.

[33] SILVA C D, SOARES T, CHEUNG N, GARCIA A, REIS D A, BRITO C. Dendritic spacing and macrosegregation affecting microhardness of an Al−Si−Mg alloy solidified under unsteady state conditions [J]. Materials Research, 2019, 22: e20190390.

[34] SEPTIMIO R S, COSTA T A, SILVA C A, VIDA T A, DAMBORENEA J, GARCIA A, CHEUNG N. Correlation between unsteady-state solidification thermal parameters and microstructural growth of Zn–8mass%Al and Zn–8mass%Al–*X*Bi tribological alloys [J]. Journal of Thermal Analysis and Calorimetry, 2020, 139(3): 1741−1761.

[35] BOUCHARD D, KIRKALDY J S. Prediction of dendrite arm spacings in unsteady and steady-state heat flow of unidirectionally solidified binary alloys [J]. Metallurgical

and Materials Transactions B, 1997, 28(4): 651−663.
[36] RUTTER J W, CHALMERS B. A prismatic substructure formed during solidification of metals [J]. Canadian Journal of Physics, 1953, 31(1): 15−39.
[37] SEKERKA R F. A stability function for explicit evaluation of the Mullins−Sekerka interface stability criterion [J]. Journal of Applied Physics, 1965, 36(1): 264−268.
[38] STJOHN D H, PRASAD A, EASTON M A, QIAN M. The contribution of constitutional supercooling to nucleation and grain formation [J]. Metallurgical and Materials Transactions A, 2015, 46(11): 4868−4885.
[39] LI H F, YANG H T, ZHENG Y F, ZHOU F Y, QIU K J, WANG X. Design and characterizations of novel biodegradable ternary Zn-based alloys with IIA nutrient alloying elements Mg, Ca and Sr [J]. Materials & Design, 2015, 83: 95−102.
[40] LIU X W, SUN J K, QIU K J, YANG Y H, PU Z J, LI L, ZHENG Y F. Effects of alloying elements (Ca and Sr) on microstructure, mechanical property and in vitro corrosion behavior of biodegradable Zn–1.5Mg alloy [J]. Journal of Alloys and Compound, 2016, 664: 444−452.
[41] LEVY G K, LEON A, KAFRI A, VENTURA Y, DRELICH J W, GOLDMAN J, AGHION E. Evaluation of biodegradable Zn−1%Mg and Zn−1%Mg−0.5%Ca alloys for biomedical applications [J]. Journal of Materials Science: Materials in Medicine, 2017, 28(11): 174.
[42] ROCHA O L, COSTA T A, DIAS M, GARCIA A. Cellular/dendritic transition, dendritic growth and microhardness in directionally solidified monophasic Sn−2%Sb alloy [J]. Transactions of Nonferrous Metals Society of China, 2018, 28(8): 1679−1686.
[43] VERISSIMO N C, BRITO C, SANTOS W L, CHEUNG N, SPINELLI J E, GARCIA A. Interconnection of Zn content, macrosegregation, dendritic growth, nature of intermetallics and hardness in directionally solidified Mg−Zn alloys [J]. Journal of Alloys and Compounds, 2016, 662: 1−10.
[44] SAVASKAN T, TURHAL M S, MURPHY S. Effect of cooling rate on structure and mechanical properties of monotectoid zinc−aluminium alloys [J]. Materials Science and Technology, 2003, 19(1): 67−74.

通过凝固冷却速率调整 Zn−1Mg−(0.5Mn, 0.5Ca)合金的显微组织和显微硬度

Talita A. VIDA[1], Cássio A. P. SILVA[1], Thiago S. LIMA[1], Noé CHEUNG[1], Crystopher BRITO[2], Amauri GARCIA[1]

1. Department of Manufacturing and Materials Engineering, University of Campinas-UNICAMP, Campinas 13083-860, SP, Brazil;
2. Campus of São João da Boa Vista, São Paulo State University-UNESP, São João da Boa Vista 13876-750, SP, Brazil

摘　要：生物可降解锌基合金，特别是添加合金元素的锌−镁(Zn−Mg)合金，已获得广泛研究以改善其力学性能和腐蚀性能。由于这些性能主要依赖于合金的显微组织，因此任何评价都应该从了解影响其形成的条件开始。本研究旨在探讨凝固冷却速率对 Zn−1Mg−(0.5Ca, 0.5Mn)(质量分数，%)合金瞬态凝固过程中显微组织演化的影响。结果表明，两种合金的显微组织均含有 3 种相：η-Zn 枝晶基体、$Zn_{11}Mg_2$ 金属间化合物和低共熔混合物中的 Zn_2Mg。$MnZn_9$ 和两种含 Ca 相($CaZn_{11}$ 和 $CaZn_{13}$)分别与 Mn 和 Ca 的添加有关。与 Zn−1Mg(质量分数，%)合金相比，添加 Mn 和 Ca 元素可以细化枝晶基体和低共熔混合物。建立冷却速率、枝晶间距或共晶间距之间的关系，从而提出实验生长规律。此外，为了研究添加 Ca 和 Mn 的效果，进行硬度测试。维氏显微硬度与二次枝晶间距之间的实验相关性表明，与二元合金相比，显微组织细化和典型的 Ca、Mn 基金属间化合物是导致硬度增加的主要原因。

关键词：Zn−Mg−(Ca, Mn)合金；凝固；冷却速率；显微组织；显微硬度

(Edited by Wei-ping CHEN)